Lab on a Chip

Accepted Manuscript

This is an *Accepted Manuscript*, which has been through the Royal Society of Chemistry peer review process and has been accepted for publication.

Accepted Manuscripts are published online shortly after acceptance, before technical editing, formatting and proof reading. Using this free service, authors can make their results available to the community, in citable form, before we publish the edited article. We will replace this *Accepted Manuscript* with the edited and formatted *Advance Article* as soon as it is available.

You can find more information about *Accepted Manuscripts* in the **Information for Authors**.

Please note that technical editing may introduce minor changes to the text and/or graphics, which may alter content. The journal's standard **Terms & Conditions** and the **Ethical guidelines** still apply. In no event shall the Royal Society of Chemistry be held responsible for any errors or omissions in this *Accepted Manuscript* or any consequences arising from the use of any information it contains.

Lab On A Chip

Lab on a Chip

Journal Article

3D Silicon Neural Probe with Integrated Optical Fibers for Optogenetic Modulation

Eric Kim [a], Hongen Tu [b], Hao Luo [c], Bin Liu [c], Shaowen Bao [d], Jinsheng Zhang [c], and Yong Xu [a,b]

Optogenetics is a powerful modality for neural modulation that can be useful for a wide array of biomedical studies. Penetrating microelectrode arrays provide a means of recording neural signals with high spatial resolution. It is highly desirable to integrate optics with neural probes to allow for functional study of neural tissue by optogenetics. In this paper, we report the development of a novel 3D neural
10 probe coupled simply and robustly to optical fibers using a hollow parylene tube structure. Device shanks are hollow tubes with rigid silicon tips, allowing the insertion and encasement of optical fibers within the shanks. The position of the fiber tip can be precisely controlled relative to the electrodes on the shank by inherent design features. Preliminary *in vivo* rat studies indicate that these devices are capable of optogenetic modulation simultaneously with 3D neural signal recording.

15 Introduction

Optogenetics as an Approach

Optogenetics is a novel approach for optically modulating neurons with unprecedented temporal and spatial resolution. Although direct stimulation of neurons by light is possible with
20 an infrared laser [1, 2], such an approach is limited both by the ability to deliver infrared laser light with high precision and by the potential damage that a sufficiently powerful laser pulse may cause. Optogenetics instead takes advantage of opsins, which are naturally occurring light sensitive proteins, to sensitize a cell to
25 light so that even low levels of light may be used to trigger depolarization or hyperpolarization [3-5]. Well established molecular biology techniques for manipulating the genetics of cells are employed to induce the expression of opsins, and it is through these techniques that cells may be induced to be light
30 sensitive in a highly specific way. Viral transfection, for example, may be used to target specific cell populations due to the specificity of viral infection mechanisms [6]. In addition to this ability to target specific populations of cells, a broad variety of known opsins allows for different effects of light on sensitized
35 cells, allowing stimulation or inhibition of these cells with different response times, sustained response durations, and sensitive light wavelengths [7]. Thanks to this additional degree of control offered by optogenetic modulation, optogenetic systems have been applied to study a wide variety of neural functions,
40 such as memory [8], behavioral disorders [9, 10], and auditory pathways [11, 12]. For investigators, optogenetics offers a powerful modality for functional investigation of neural networks, with greatly improved spatial and temporal resolution thanks to the nature of light [2, 13, 14], biologic specificity thanks to
45 microbiologically induced opsins [15-17], and no direct channel cross-talk.

Engineering Approaches to Optogenetic Modulation and Recording

Currently, many technical approaches to optogenetics have been
50 developed [7, 18]. Some methods have focused on the use of light alone without the aid of implanted delivery mechanisms. Bovetti et al. used liquid crystal spatial light modulators to direct light through microscope objectives and onto tissue surfaces with high spatial and temporal precision [19]. Szabo et al. used highly
55 controlled light stimulation and recording from a brain-surface attached fiber bundle for both light delivery and acquisition of fluorescence for observing neural signals [20]. Both of these systems deliver light through the surface of the brain with the aid of external optic equipment. Another approach has used arrays of
60 micro-LEDs integrated into an ECoG (electrocorticography) electrode array at the surface of the brain, allowing for lateral selectivity of light exposure without the need for an external light source [21-23]. Kim et al. used a novel technique to form arrays of interconnected, ultrathin micro-LEDs that could be placed
65 conformally on the surface of the brain. Kwon et al. incorporated SU-8 (a light curable polymer) penetrating waveguides attached at their bases to a grid of micro-LEDs to allow for light delivery at some depth beneath the surface of the brain [24], a capability otherwise lacking in surface mounted light sources.
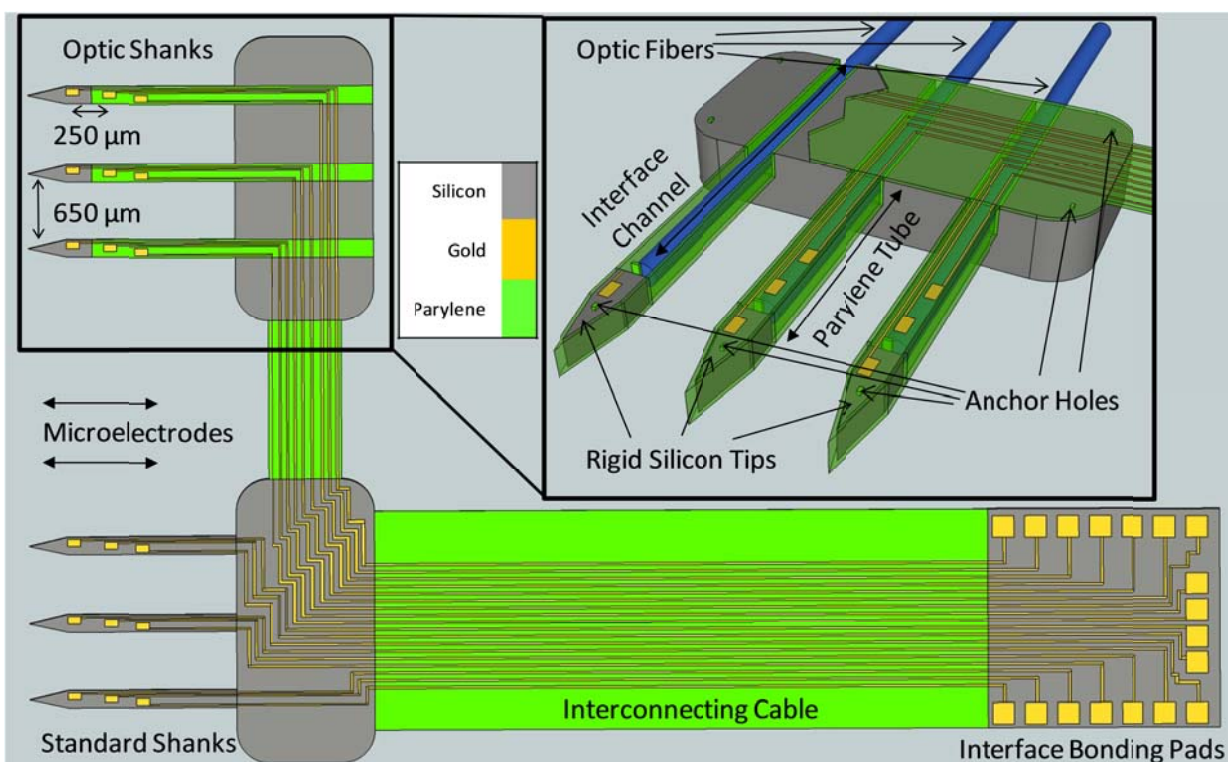
Fig. 1. 3D Schematic of the device design showing the topside view of the device prior to folding assembly. (insert) close-up schematic of the shank array with integrated optic fibers

In order to improve optogenetic stimulation of deeper structures, implantable optical fibers have been used to transmit light to deeper locations [25], but this approach provides limited recording options. The simplest manifestation of this approach that has been used is the implantation of a separate optical fiber and micro wire for modulation and recording [26]. Ozden et al. developed a penetrating optical fiber with integrated recording capabilities by means of a patterned insulated gold coating on the outside of the fiber, allowing for depth recording concurrent with optical modulation [27]. This "optrode" concept was expanded into a small optrode array using microfabrication methods by Chen et al. [28]. Optical fibers have also been patterned by focused ion beam milling to provide individually addressable optical exit ports on a single optical fiber [29]. To expand recording capabilities, optic fibers have also been coupled to silicon neural probes. Royer et al. manually glued an optical fiber to a Michigan Probe using complex microassembly techniques to manipulate and properly align the components [30]. Blackrock's Utah arrays have also been coupled to sharpened optrodes inserted into a hole in the center of the array and then secured [31].

Using microfabrication techniques, penetrating microelectrode arrays with integrated optical waveguides for light delivery have been developed. Fan et al integrated a single oxynitride waveguide into a silicon probe, providing light delivery to the region immediately adjacent the probe's electrodes [32]. This device relied on a coupled optical fiber as a light source. Yoojin et al. took this a step further, integrating a network of interconnected SU-8 polymer waveguides on a multi-shank silicon neural probe that allows multisite light delivery from a single optical fiber source [33]. In order to reduce device profile and enable individually addressable control of light delivery ports,

Schwaerzle et al. created a multi-shank silicon neural probe with multiple separate SU-8 waveguides that were each coupled to an on-chip micro-LED light source [34]. Zorzos et al. expanded waveguide delivery of light into 3D with a slotted modular silicon device [35]. Individual 2D shanks with multiple waveguides and light delivery sites along their length were slotted into a brace by micro assembly, providing a truly 3D grid of light delivery sites. However, this device has no microelectrodes and uses a light projection system as a source, which complicates its use in moving animal tests.

These approaches have shown successes, but there is still a great need for optogenetic probes with 3D mapping capability. We have previously reported a novel 3D neural probe technology based on a silicon island structure and a simple, robust folding assembly procedure [36-38]. Specifically, planar devices consisting of multiple silicon islands were fabricated on silicon wafers using a flexible skin process [39-41]. Every silicon island carried a 2D multi-shank electrode array. The silicon islands were interconnected by a parylene C layer, which was embedded with metal traces for inter-island communication. The planar multi-island device was then assembled into 3D electrode arrays by a simple folding and stacking process. The simplified assembly and packaging process leads to higher yield and lower cost for these 3D electrode arrays.

This is a very versatile platform which allows the integration of various features and functions. For example, we have demonstrated novel probes possessing both rigid silicon and flexible parylene tube regions in their shanks. Such probes aim to reduce mechanical mismatch and simultaneously retain the easy implantation procedures of conventional rigid probes [42]. Based on these novel structures, we have proposed in this paper a simple,
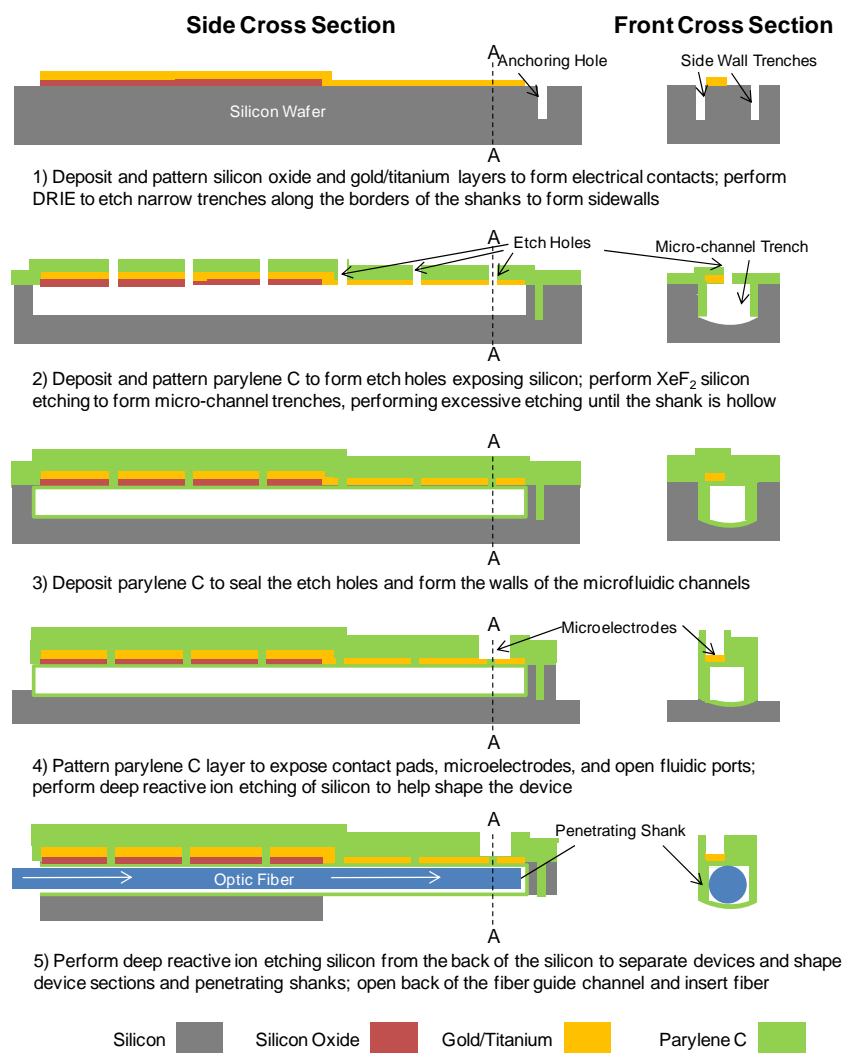
Fig. 2. General fabrication protocol for our optical fiber integrated 3D neural probes. The process is very similar to the one used for our previously reported hollow parylene tube shanks. Please note that we do not show the fabrication of the flexible cables and the interface island for simplicity.

effective way of reliably and precisely integrating optical fibers with fully assembled 3D penetrating microelectrode neural probes. Our parylene tube structures, if extended from the silicon tip through the bulk of the silicon island to exit on the non-shank
5 edge of the silicon island, can be used to guide the insertion of an optical fiber, as well as acting as a highly robust encasement that precisely fixes the fiber tip with respect to the electrodes. A 3D schematic of this design can be seen in figure 1.

Fabrication

10 The fabrication process of the design pictured in figure 1 is summarized in figure 2. This process is similar to the ones we have previously reported [36-38, 43]. A batch of devices was fabricated on a <100> mono-crystalline double-side polished 300 µm thick 4" silicon wafer. A layer of silicon dioxide 300 nm thick
15 was first grown via wet thermal oxidation and patterned by standard photolithographic techniques. This layer serves as a robust dielectric layer insulating the metal of the device from the semiconductive silicon in regions of the device where silicon is

not removed, as well as providing a bottom side encapsulation to
20 traces passing through the flexible interconnects. A thin film of metal, 20 nm/250 nm titanium/gold, was then deposited by electron beam evaporation (Temescal Model BJD-1800 e-beam evaporator). Using standard photolithography techniques the metal was patterned to form microelectrodes, contact pads, and
25 traces. These steps are summarized in figure 2-1.

Deep reactive ion etching (DRIE based on Bosch process in a Plasma-Therm 790 SLR) was used to etch 8 µm wide 150 µm deep trenches and holes in the silicon to act as molds for the formation of parylene sidewalls and mechanical anchoring holes
30 for the parylene film. A 5-7 µm layer of parylene C was then deposited by thermally activated chemical vapor deposition (CVD) using a Specialty Coating Systems CVD chamber (SCS PDS 2010). Parylene C tends to have poor adhesive strength to silicon and silicon oxide. In order to prevent this from becoming
35 an issue, silane adhesion promotor was used. Furthermore, trenches and holes previously etched in silicon by DRIE were filled by the conformal layer of parylene as its thickness
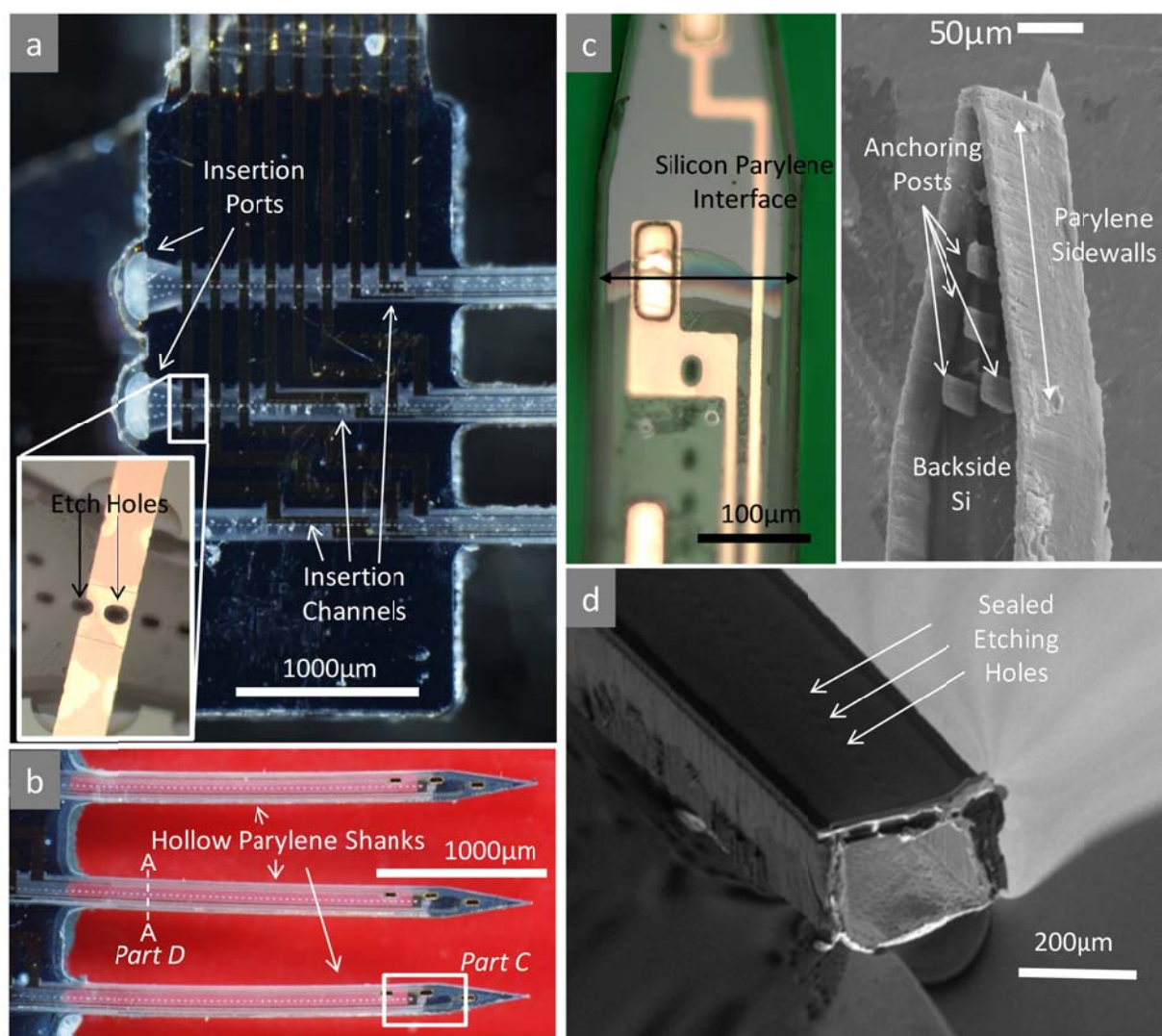
Fig. 3. Images of the fabricated device. (a) Micrograph of the hollow channels that lead from the insertion ports to the hollow shanks. (inset) micrograph showing the metal trace passing over the fiber interface channel and intersecting the line of sealed etch holes (b) Image of the hollow parylene shanks of the device. (c) silicon tip of the device shanks (left) micrograph showing the silicon parylene interface from the top side where the hollow parylene tube ends and the rigid silicon tip begins. (right) SEM image showing the backside of a shank from a similar device which has been over-etched to reveal parylene anchors. (d) SEM of the cut cross section of the parylene tube structure. Note that the rough edge was due to cutting.

surpassed half the width of the cavities. These parylene structures helped to provide robust mechanical anchoring of parylene to the silicon, as well as providing parylene walls for limiting the lateral extent of optical fiber channel formation. These parylene ⁵ anchoring posts and sidewalls are shown in figure 3c. After this, a linear sequences of etch holes 8 μm by 20 μm large and 20 μm apart were patterned in the parylene layer by oxygen reactive ion etching (RIE, DryTech RIE 184) and an aluminum mask, exposing silicon for XeF_2 etching. Note that the holes in the ₁₀ Au/Ti layer are of smaller size (at smallest 8 μm × 8 μm) than the width of the metal traces and so do not cause discontinuities (see inset of figure 3a). Silicon was then etched through the etch holes by XeF_2 gas. Due to the isotropic nature of the XeF_2 etching, continuous trenches with a lateral dimension of roughly 150 μm × ₁₅ 150 μm were undercut in the silicon substrate beneath the parylene layer. These steps are summarized in figure 2-2.

In order to seal the microchannels, 10 μm of parylene C was deposited by CVD. Due to the highly conformal deposition of parylene, the walls of the trenches were conformally coated with ₉₀ parylene, forming parylene microchannels for fiber insertion [36-38, 42, 43]. It is worth noting that parylene walls formed by refill of the DRIE etched trenches during the deposition of the first layer of parylene form the lateral walls of the channel and are thickened during the second parylene deposition. This is in contrast to the ₉₅ bottom of the channel which forms only with the second deposition. At this point, parylene on the top surface of the silicon reaches 15-17 μm thick, the top of the channels are 20-22 μm thick, the sidewalls of the channels are 12 μm thick, and the bottom wall 4 μm thick. These steps are summarized in figure 2-₁₀₀ 3.

Next, parylene was again patterned using oxygen RIE and an aluminum mask to expose gold contact pads, microelectrodes,

and the silicon surrounding the devices. Front-side DRIE was performed etching silicon around the devices to a depth of 150 μm in order to shape the device and shanks. During this step, silicon was etched away from the area around the shanks as well as all around the outer boundaries of the device. These steps are summarized in figure 2-4. In figure 2-5, the wafer was etched from the backside by DRIE until the bottom of the 150 μm deep cavities formed during the frontside etch are reached, fully releasing the shaped shanks and the device from the surrounding silicon.

The fabricated devices consist of one interfacing island and two shank islands, each carrying a 3 × 3 electrode array on its shanks, as schematically illustrated in figure 1. These electrode arrays are comprised of three penetrating shanks with three electrodes along their lengths. Each electrode measures 25 μm × 75 μm. The electrodes are spaced 250 μm apart along the shanks and the shanks are positioned 650 μm apart. For simplicity of insertion of optical fibers with these prototype devices, only the three shanks on the island farthest from the interface cable were designed to be hollow parylene tubes for optical fibers. In the future the remaining three shanks on the other island may be made hollow parylene tubes with a slight redesign moving the interface cable which currently blocks potential insertion ports. Images of the fabricated device can be seen in figure 3. Enlarged parylene insertion channels, shown in figure 3a, can be seen from the top of the device head, extending from insertion ports at the back of the silicon island to the base of the hollow parylene shanks. A 20X microscopy image of a metal trace as it crosses the line of XeF_2 etch holes can be seen in the inset, showing that the metal traces remain continuous. A detailed image of the hollow parylene shanks, which connect to the insertion channels on the silicon island, can be seen in figure 3b. The rigid silicon tips of the shanks, which allow for ease of insertion, can also be observed. The parylene walls of the shanks are transparent to visible light [44, 45], allowing for the effective emission of light from the fiber tips. The left image of figure 3c shows a microscopy image of the interface between the hollow parylene region and the rigid silicon tip. This interface lies underneath the top layer of parylene. The right SEM image shows the backside of the silicon tip from a similar device with the silicon excessively etched to reveal parylene sidewalls and parylene posts that act as mechanical anchors. Figure 3d shows a scanning electron microscopy (SEM) image of the cross section of one of these hollow parylene tube shanks that was used to encase the optical fiber. The position of the cross section is marked by the dashed line A-A on the central shank in figure 3b. A row of sealed etch holes can be observed along the top that were used during fabrication to expose silicon for isotropic etching by XeF_2 gas. The roughened edges of the tube are the result of damage from the cutting of the shank by a razor blade. Curved distortions surrounding the tube are the result of charging effects on the surface of the parylene during SEM imaging.

Assembly and Packaging

Assembly

After releasing, the 3D grid was assembled by folding the 2D shank islands and stacking them on top of each other using the same procedure as our previous devices [36-38, 43]. When fully assembled, the distance between the shank groups is 600 μm, producing a 2 × 3 × 3 grid of electrodes. They were bonded together using marine epoxy. The bending of the interconnecting cables has demonstrated no breakage of the metal traces, which was confirmed by impedance spectroscopy readings after assembly. Our original solid silicon shank neural probes [36-38, 43] have demonstrated recording stability for at least 4 weeks, suggesting that these interconnects are fairly reliable. The folded device prior to coupling of optical fibers can be seen in figure 4a. Devices were then packaged for readout by wire-bonding to a custom printed circuit board (PCB) connected to an Omnetics connector. Exposed terminals from the connector and metal traces on the PCB were covered in marine epoxy. At this point, the insertion points for the optical fibers on the silicon island holding the shanks were mechanically opened by a fine tipped needle. The opened insertion ports can be seen in figure 4b. 125 μm diameter, 50 μm core multimodal optical fibers (Thorlabs,
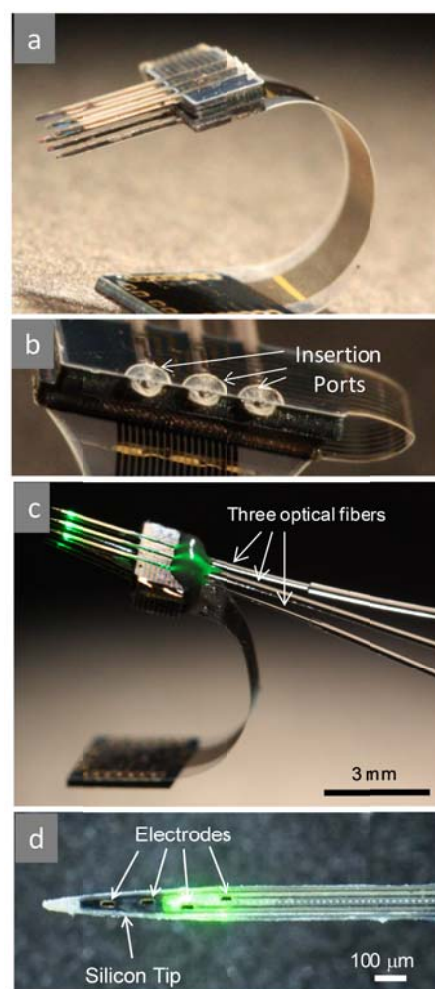

Fig. 4. Images of the assembled 3D MEA. (a) Device after folding assembly of the 3D grid of electrodes, prior to optic fiber coupling. (b) Image of the open fiber insertion ports. (c) A device coupled to three optic cables showing green laser light emitting from the shank tips adjacent to electrodes. Note that our in vivo studies used only a single shank coupled to a fiber. (d) Micrograph of a single parylene tube shank coupled to an active optic fiber (green light emitting).
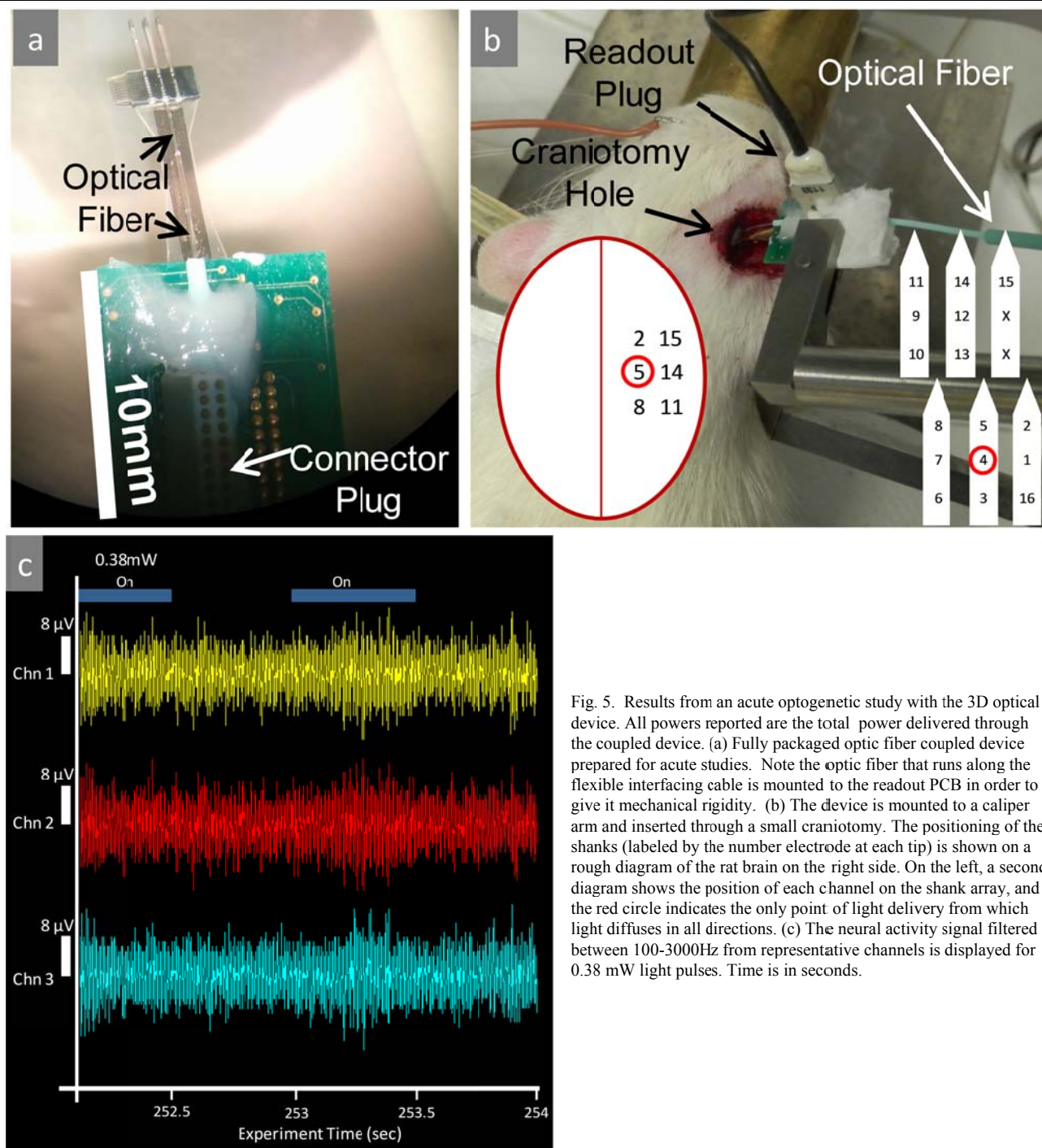
Fig. 5. Results from an acute optogenetic study with the 3D optical device. All powers reported are the total power delivered through the coupled device. (a) Fully packaged optic fiber coupled device prepared for acute studies. Note the optic fiber that runs along the flexible interfacing cable is mounted to the readout PCB in order to give it mechanical rigidity. (b) The device is mounted to a caliper arm and inserted through a small craniotomy. The positioning of the shanks (labeled by the number electrode at each tip) is shown on a rough diagram of the rat brain on the right side. On the left, a second diagram shows the position of each channel on the shank array, and the red circle indicates the only point of light delivery from which light diffuses in all directions. (c) The neural activity signal filtered between 100-3000Hz from representative channels is displayed for 0.38 mW light pulses. Time is in seconds.

FG050LGA) were inserted to their fullest extent and fixed in place by marine epoxy placed around the insertion port.

Coupled optical fibers were connected to a green Laser Centry SLOC diode-pumped solid-state (DPSS) laser via a FC/PC connector. Lasers were activated to varying output power levels (above 1mW), and microscopy images were taken of the light exiting the devices adjacent to the gold microelectrodes. The fiber coupled device can be seen in figure 4c, where three optical fibers have been coupled into three separate shanks on this six shank 3D device. Green light can be seen emitting from the tips of the fiber coupled shanks. With this design, the relative position between

the optical fiber and electrodes can be precisely controlled. As shown in figure 4d in one embodiment, the light emits between the 2nd and 3rd electrodes, just proximal to the silicon tip. The parylene encasement provides little barrier to the exiting light, as it shows very low absorption of light within the visible spectrum [44, 45].

Impedance spectroscopy was performed on the devices using a high precision meter. The device microelectrodes were immersed in 1X phosphate buffered saline (PBS) and measurements taken versus a platinum counter electrode between 200Hz and 20000Hz. Microelectrodes tended to have an impedance of 1MOhm at 1kHz, comparable to our previous solid silicon shank

devices. To characterize coupling efficiency, the total power of the light emitted from the tip was measured in an integrating sphere light sensor (Thorlabs S140C) and compared to the power from the bare fiber. The coupling efficiency was found to be -5dB within the measured range between 80µW and 4.8mW input power. Bench-top tests measuring the voltage across device
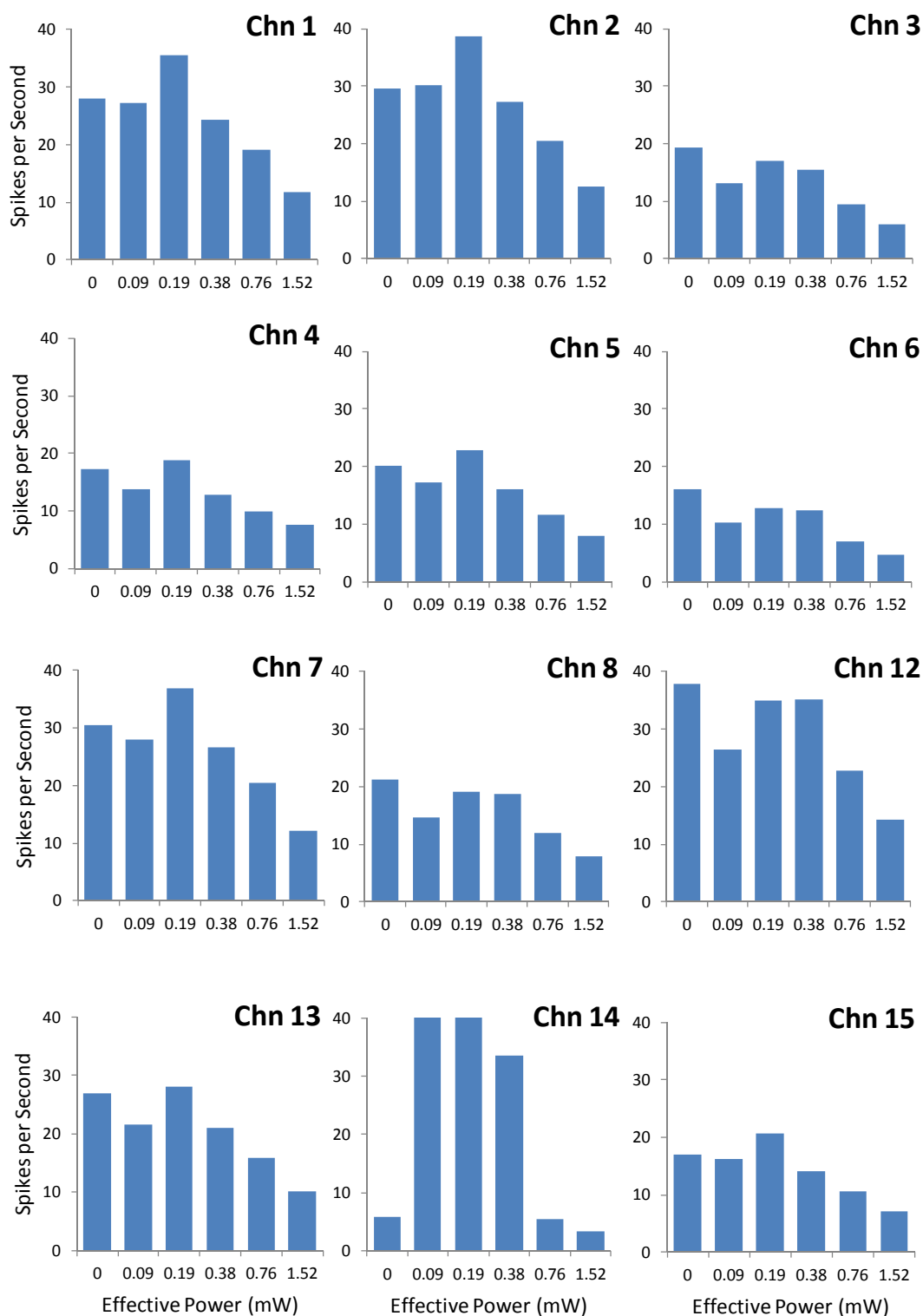

Fig. 6. In vivo recorded average spontaneous spiking rates presented per light power level. These average spiking rates were computed for the entire 5 minute recording for each power level, including both light on and light off intervals. Although there is considerable variance, a distinct decline in spontaneous spiking can be observed as power increases. Please note that channels 9, 10, 11, and 16 were not included because they did not record a signal with sufficient signal to noise ratio to extract spiking information, presumably because they were broken.

electrodes in PBS versus a platinum counter electrode showed no voltage response to 550nm light impulses up to 32mW, suggesting that the photoelectric effect likely will not contribute to voltage signal artifacts during recording.

Animal Tests

All *in vivo* experimental protocols were approved by the Wayne State University Institutional Animal Care and Use Committee under protocol number A04-10-13 prior to implementation. We performed *in vivo* tests in male Sprague Dawley rats. Two weeks prior to surgery, we exposed the skull along the right temporal ridge, drilled three evenly spaced 0.6mm holes above the auditory cortex, and performed microinjection at each of these sites. An adeno-associated virus vector (titer 4x1012 TU/ml) of arhaerhodopsin from the Halorubrum strain TP009 (ArchT, Gene Therapy Center Vector Core, The University of North Carolina at Chapel Hill) targeted to pyramidal neurons was used. Each injection was performed in two stages, with 0.5 µl of viral suspension injected at the depth of 900 µm from the dura and 0.5 µl injected at 600 µm. Following injection, the glass micropipette remained in place for 5 minutes.

Anesthesia was induced by ventilation of a mixture of air (0.4 liters/min) and isoflurane (2-3% v/v) via a chamber followed by a mask. A craniotomy was performed to provide access to the right auditory cortex. Skull, temporal muscle, and dura was removed referencing anatomic landmarks to reveal the cortex. A Kopf Model 1460-61 micromanipulator was used to lower the 3D neural probe until it was 0.8-1.0 mm below the cortical surface to position microelectrodes in layers 1-3, 4, and 5-6 of the right superficial auditory cortex. During the experiment, regular irrigation with warm sterile saline was used to protect the exposed tissue.

For optogenetic recording, neural probe channels were connected to an amplifier and real-time processing system (RZ2, Tucker Davis Technologies) with a 25 kHz sampling rate and a 100-3000 Hz bandpass filter. Although the device has an array of 18 electrodes total, our recording acquisition system only allows 16 channel recording. As a result, only 16 channels were connected for recording. Optics were connected to a 550nm Laser Centry DPSS laser module via a multimodal optical fiber and the total input power of the laser varied between recordings. 500 ms optical pulses with 500 ms inter-pulse periods were controlled by our stimulation equipment via an analog TTL control interface in the laser. During each recording period, spontaneous multi-unit spiking was acquired for 5 minutes with a fixed pulsed power level. A zero pulsed power level recording was included as a control.

Preliminary acute *in vivo* optogenetic tests with our fiber optic 3D neural probes have been performed in rat auditory cortex using arhaerhodopsin, which causes hyperpolarization (and thus inhibition) via a proton ion channel mechanism [46, 47]. In figure 5a, a fully packaged 3D device is pictured, ready for implantation and acute studies. Although three fibers were inserted into the demonstration device imaged in figure 4c, for simplicity only a single fiber was inserted into the central shank of the *in vivo* device tested. Figure 5b shows the device mounted to the end of a micromanipulator arm, which was used to lower the device shanks into the superficial cerebral cortex through a small craniotomy hole in the rat's skull. A divided red oval on the figure serves as a rough diagram of the rat cerebral cortex. The numbers indicate the positions of shanks, with the numbers reflecting the electrode closest to the tip. A red circle indicates the shank with the integrated optical fiber. The complete electrode number map is also shown as an inset, with the red circle indicating the point of light emission. We took recordings of spontaneous activity with varying levels of pulsed laser power. After signal conditioning, recordings from individual channels are examined for spiking by means of thresholding and average spikes per second determined for each signal. A representative portion of the conditioned signals during the 0.38mW power pulsed light condition used to detect and quantify spiking activity is shown in figure 5c. Both synchronized and desynchronized spontaneous spiking activity (in the form of bursts) can be observed, indicating separate recording from individual channels. Note that the broad regular spike clusters synchronized to each channel are breathing artifacts. A clear difference in spiking rate was not observed between pulse and inter-pulse intervals within each channel. However, a clear difference was observed in the average spiking rate (including both pulse and inter-pulse intervals) between each power level for individual channels. The lack of obvious pulse effect on activity within each recording could be due to an inter-pulse interval that was too short to observe restoration of normal activity. This could also have been due to the confounding signals from multiple neurons from this multi-unit recording. Figure 6 shows the average spiking rate per light power level recorded by each active electrode. Please note that channels 9, 10, 11, and 16 were excluded due to low signal to noise ratios that prevented spike quantification, possibly due to damage or mis-wiring during assembly. The averaged spiking rates between all electrodes decreases with increasing laser power, with statistically significant separation ($p < 0.01$) achieved at 0.76 mW and 1.52 mW total delivered power (using a two sample t-test for unequal variances to compare groups to the initial zero power condition). It should be noted that the power levels were attempted in the order 0, 0.38, 0.19, 0.09, 0.76, and 1.52 mW, not in numeric order. All light power levels are reported in direct power delivery to the neural tissue accounting for the 5dB coupling loss of the device. A trend can be observed of decreasing spontaneous spiking activity with increasing light simulation power. This trend is consistent with the expected inhibition induced by arhaerhodopsin. Unexpectedly, the multi-channel recording seems to show weak location specific optical modulation of neural activity, instead showing more universal optical modulation. This may be the result of a number of issues, including weak optogenetic transfection, non-optimal positioning of micro injection of transfection vector, confounding multi-unit signals, and insufficiently small increments in optical power levels to properly identify individual modulation thresholds for different locations within the grid. This unexpected behaviour will be examined in future *in vivo* studies.

In order to achieve threshold power for optogenetic modulation, a range around 1 mW/mm² has been reported to be required [48]. With a 100 mW laser at our disposal, the required power density for stimulation can be easily achieved. In our preliminary acute *in vivo* optogenetic studies, we found that 0.76 mW and 1.52 mW total delivered power showed statistically significant optogenetic

effects. Clear spontaneous activity recording from individual microelectrodes was observed as it has been with our previous devices, demonstrating the 3D recording capabilities of this device. Combined with an observable suppression of activity at higher light power injection, this study has demonstrated our optical fiber integrated 3D implantable neural probe based on our hybrid silicon-parylene design. It should be emphasized that these preliminary *in vivo* results are simply intended as validation of device functionality. More comprehensive *in vivo* studies are planned to provide more rigorous animal data.

Discussion

Our novel device provides improvements on the recording capabilities and assembly simplicity, precision, and robustness compared to other optical fiber integrated devices. Although 2D silicon devices can be stacked to form a 3D array, our approach provides another simple yet robust approach to the assembly of a 3D electrode array. Further, the integration of an optical fiber in other devices is usually reliant on micro assembly techniques for precisely positioning the fiber with respect to the microelectrode array. Thanks to the parylene tube structures, our approach precisely and robustly positions optical fibers with respect to the electrode array without the need of micro manipulating aids. However, our technology does not seek to provide the same high density multi-site optical modulation that integrated waveguides offer. In our case, although the integration of multiple optical fibers is possible, it would significantly complicate device implantation and chronic use. In addition, the insertion of only a single fiber per shank restricts the total number of possible light delivery sites to one per shank. Though still constrained by the same limits as other optical fiber based devices, this novel approach offers advantages for optical fiber integration into a true 3D array of recording electrodes for 3D neural activity mapping of deeper structures within the superficial cortical layers. We are currently working on novel waveguide and optical switching technology that could enable high density multi channel optical stimulation.

Conclusions

Using methods that we have previously reported to generate parylene-walled microchannels and hollow parylene tube shanks [36, 38, 42, 43], we have demonstrated a 3D recording neural probe with simply and robustly integrated optical fibers for optogenetic study. Microchannels in the device guide optical fibers from insertion points on the silicon island into hollow parylene shanks, which encase fibers and hold the light emitting tips adjacent to recording microelectrodes in a highly precise and robust fashion. In a preliminary *in vivo* study in the auditory cortex of a rat using the opsin arhaerhodopsin transfected by an adeno-virus vector via micro-injection, clear neural electrical activity was recorded in a 3D array of electrodes, sufficient to quantify the spontaneous spiking rate at individual electrodes. Suppression of spontaneous spiking rates was noted with increasing pulsed light power exposure, offering a preliminary validation of the functionality of these devices. In the future, we will seek to integrate waveguides into our 3D neural probe technology for high-density multi-site optogenetic stimulation.

Notes and references

[a] The biomedical engineering department of Wayne State University, Detroit, MI 48202, USA.
[b] The electrical engineering department of Wayne State University, Detroit, MI 48201, USA.
[c] The department of otolaryngology at the Wayne State University School of Medicine, Detroit, MI 48202, USA.
[d] The Helen Wills Neuroscience Institute, University of California, Berkeley, Berkeley, CA 94720, USA.

1. J. Wells, C. Kao, E. D. Jansen, P. Konrad and A. Mahadevan-Jansen, BIOMEDO, 2005, **10**, 064003-064003-064012.
2. J. Wells, P. Konrad, C. Kao, E. D. Jansen and A. Mahadevan-Jansen, Journal of Neuroscience Methods, 2007, **163**, 326-337.
3. E. S. Boyden, F. Zhang, E. Bamberg, G. Nagel and K. Deisseroth, Nature neuroscience, 2005, **8**, 1263-1268.
4. F. Zhang, L. P. Wang, E. S. Boyden and K. Deisseroth, Nature methods, 2006, **3**, 785-792.
5. F. Zhang, L. P. Wang, M. Brauner, J. F. Liewald, K. Kay, N. Watzke, P. G. Wood, E. Bamberg, G. Nagel, A. Gottschalk and K. Deisseroth, Nature, 2007, **446**, 633-639.
6. L. S. Hamilton, J. Sohl-Dickstein, A. G. Huth, V. M. Carels, K. Deisseroth and S. Bao, Neuron, 2013, **80**, 1066-1076.
7. O. Yizhar, Lief E. Fenno, Thomas J. Davidson, M. Mogri and K. Deisseroth, Neuron, 2011, **71**, 9-34.
8. I. Goshen, Trends in neurosciences, 2014.
9. S. A. Allsop, C. M. Vander Weele, R. Wichmann and K. M. Tye, Frontiers in behavioral neuroscience, 2014, **8**, 241.
10. K. Cho and V. S. Sohal, Human molecular genetics, 2014.
11. S. Q. Lima, T. Hromádka, P. Znamenskiy and A. M. Zador, PLoS ONE, 2009, **4**, e6099.
12. V. H. Hernandez, A. Gehrt, K. Reuter, Z. Jing, M. Jeschke, A. Mendoza Schulz, G. Hoch, M. Bartels, G. Vogt, C. W. Garnham, H. Yawo, Y. Fukazawa, G. J. Augustine, E. Bamberg, S. Kugler, T. Salditt, L. de Hoz, N. Strenzke and T. Moser, The Journal of clinical investigation, 2014, **124**, 1114-1129.
13. M. M. Sidor and C. A. McClung, Frontiers in behavioral neuroscience, 2014, **8**, 41.
14. K. M. Tye and K. Deisseroth, Nature reviews. Neuroscience, 2012, **13**, 251-266.
15. F. Zhang, J. Vierock, O. Yizhar, L. E. Fenno, S. Tsunoda, A. Kianianmomeni, M. Prigge, A. Berndt, J. Cushman, J. Polle, J. Magnuson, P. Hegemann and K. Deisseroth, Cell, 2011, **147**, 1446-1457.
16. J. Mattis, K. M. Tye, E. A. Ferenczi, C. Ramakrishnan, D. J. O'Shea, R. Prakash, L. A. Gunaydin, M. Hyun, L. E. Fenno, V. Gradinaru, O. Yizhar and K. Deisseroth, Nature methods, 2012, **9**, 159-172.
17. G. Nagel, T. Szellas, W. Huhn, S. Kateriya, N. Adeishvili, P. Berthold, D. Ollig, P. Hegemann and E. Bamberg, Proceedings of the National Academy of Sciences, 2003, **100**, 13940-13945.
18. A. M. Aravanis, L.-P. Wang, F. Zhang, L. A. Meltzer, M. Z. Mogri, M. B. Schneider and K. Deisseroth, Journal of Neural Engineering, 2007, **4**, S143.
19. S. Bovetti and T. Fellin, Journal of Neuroscience Methods, 2015, **241**, 66-77.
20. V. Szabo, C. Ventalon, V. De Sars, J. Bradley and V. Emiliani, Neuron, 2014, **84**, 1157-1169.
21. Y. Iwai, S. Honda, H. Ozeki, M. Hashimoto and H. Hirase, Neuroscience Research, 2011, **70**, 124-127.
22. G. Nir, P. Vincent, S. G. Matthew, T. K. Gordon, N. Konstantin, M. Brian, P. Rolando Berlinguer, G. Zheng, M. D. Emmanuel, A. A. N.

Mark, D. D. Martin, B. Juan and D. Patrick, Journal of Neural Engineering, 2010, **7**, 016004.

23. K. Y. Kwon, B. Sirowatka, A. Weber and W. Li, IEEE transactions on biomedical circuits and systems, 2013, **7**, 593-600.

24. K. Y. Kwon, A. Khomenko, M. Haq and W. Li, Conference proceedings : ... Annual International Conference of the IEEE Engineering in Medicine and Biology Society. IEEE Engineering in Medicine and Biology Society. Annual Conference, 2013, **2013**, 249-252.

25. D. R. Sparta, A. M. Stamatakis, J. L. Phillips, N. Hovelso, R. van Zessen and G. D. Stuber, Nature protocols, 2012, **7**, 12-23.

26. V. Gradinaru, K. R. Thompson, F. Zhang, M. Mogri, K. Kay, M. B. Schneider and K. Deisseroth, J. Neurosci., 2007, **27**, 14231-14238.

27. I. Ozden, J. Wang, Y. Lu, T. May, J. Lee, W. Goo, D. J. O'Shea, P. Kalanithi, I. Diester, M. Diagne, K. Deisseroth, K. V. Shenoy and A. V. Nurmikko, Journal of Neuroscience Methods, 2013, **219**, 142-154.

28. S. Y. Chen, W. H. Pei, Q. Gui, Y. F. Chen, S. S. Zhao, H. Wang and H. D. Chen, Journal of Neural Engineering, 2013, **10**.

29. F. Pisanello, L. Sileo, Ian A. Oldenburg, M. Pisanello, L. Martiradonna, John A. Assad, Bernardo L. Sabatini and M. De Vittorio, Neuron, 2014, **82**, 1245-1254.

30. S. Royer, B. V. Zemelman, M. Barbic, A. Losonczy, G. Buzsaki and J. C. Magee, European Journal of Neuroscience, 2010, **31**, 2279-2291.

31. J. Zhang, F. Laiwalla, J. A. Kim, H. Urabe, R. Van Wagenen, Y. K. Song, B. W. Connors, F. Zhang, K. Deisseroth and A. V. Nurmikko, Journal of Neural Engineering, 2009, **6**, 055007.

32. W. Fan, S. Eran, I. Maesoon, C. Il-Joo, Y. Eui-Sung, B. György, D. W. Kensall and Y. Euisik, Journal of Neural Engineering, 2013, **10**, 056012.

33. S. Yoojin, H. J. Lee, K. Dohee, K. Yun Kyung, Y. Eui-Sung, K. Ji Yoon, C. Nakwon, K. Tae Geun and C. Il-Joo, MEMS neural probe array for multiple-site optical stimulation with low-loss optical waveguide by using thick glass cladding layer, 2014.

34. M. Schwaerzle, K. Seidl, U. T. Schwarz, O. Paul and P. Ruther, Ultracompact optrode with integrated laser diode chips and SU-8 waveguides for optogenetic applications, 2013.

35. A. N. Zorzos, J. Scholvin, E. S. Boyden and C. G. Fonstad, Opt. Lett., 2012, **37**, 4841-4843.

36. Y. Li, J. John, J. Loeb and Y. Xu, presented in part at the Hilton Head Workshop 2010: A Solid-State Sensors, Actuators and Microsystems Workshop Hilton Head Island, SC June 6 - 10, 2010, 2010.

37. J. John, Ph.D., Wayne State University, 2012.

38. J. John, Y. F. Li, J. S. Zhang, J. A. Loeb and Y. Xu, J. Micromech. Microeng., 2011, **21**.

39. Y. Xu, J. Clendenen, S. Tung, F. Jiang and Y.-C. Tai, Underwater flexible shear-stress sensor skins, Maastricht, The Netherlands, 2004.

40. Y. Xu, F. Jiang, Y.-C. Tai, A. Huang, C.-M. Ho and S. Newbern, Sensors & Actuators, 2003, **105**, 321-329.

41. Y. Xu, Y.-C. Tai, A. Huang and C.-M. Ho, Journal of Microelectromechanical Systems, 2003, **12**, 740-747.

42. E. G. R. Kim, J. K. John, H. Tu, Q. Zheng, J. Loeb, J. Zhang and Y. Xu, Sensors and Actuators B: Chemical, 2014, **195**, 416-422.

43. J. K. John, E. Kim, H. Tu, J. Zhang, J. A. Loeb and Y. Xu, Multifunctional chronic 3D electrode arrays based on a simple folding process, Barcelona. Spain, 2013.

44. Parylene Technical Data Sheet, Specialty Coating Systems, Inndianapolis.

45. O. I. Szentesi and E. A. Noga, Applied optics, 1974, **13**, 2458-2459.

46. B. Y. Chow, X. Han, A. S. Dobry, X. Qian, A. S. Chuong, M. Li, M. A. Henninger, G. M. Belfort, Y. Lin, P. E. Monahan and E. S. Boyden, Nature, 2010, **463**, 98-102.

47. X. Han, B. Y. Chow, H. Zhou, N. C. Klapoetke, A. Chuong, R. Rajimehr, A. Yang, M. V. Baratta, J. Winkle, R. Desimone and E. S. Boyden, Frontiers in systems neuroscience, 2011, **5**, 18.

48. H. Cao, L. Gu, S. K. Mohanty and J. C. Chiao, IEEE transactions on bio-medical engineering, 2013, **60**, 225-229.